

Spatiotemporally Programmable Metasurfaces via Viscoelastic Shell Snapping

Yuzhen Chen¹, Tianzhen Liu^{1,2}, and Lihua Jin¹

¹University of California Los Angeles

²Southeast University

December 22, 2021

Abstract

Many species can dynamically alter their skin textures to enhance their motility and survivability. Despite the enormous efforts on designing bio-inspired materials with tunable surface textures, developing spatiotemporally programmable and reconfigurable textural morphing without complex control remains challenging. Here we propose a design strategy to achieve metasurfaces with such properties. The metasurfaces comprise an array of unit cells with broadly tailored temporal responses. By arranging the unit cells differently, the metasurfaces can exhibit various spatiotemporal responses, which can be easily reconfigured by disassembling and rearranging the unit cells. Specifically, we adopt viscoelastic shells as the unit cells, which can be pneumatically actuated to a concave state, and recover the initial convex state some time after the load is removed. We computationally and experimentally show that the recovery time can be widely tuned by the geometry and material viscoelasticity of the shells. By assembling such shells with different recovery time, we build metasurfaces with pre-programmed spatiotemporal textural morphing under simple pneumatic actuation, and demonstrate temporal evolution of patterns, such as digit numbers and emoji, and spatiotemporal control of friction. This work opens up new avenues in designing spatiotemporal morphing metasurfaces that could be employed for programming mechanical, optical and electrical properties.

Corresponding author: Lihua Jin, Email: lihujin@seas.ucla.edu

ToC Figure

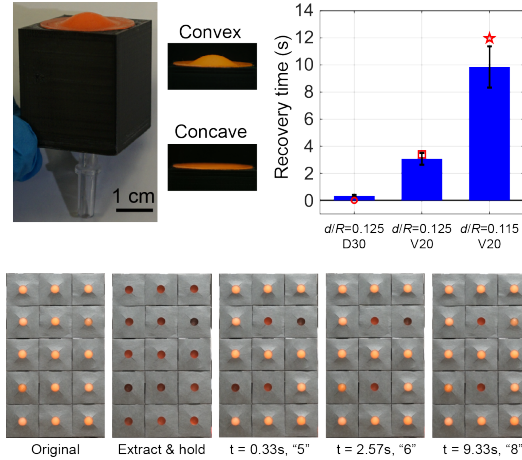


Figure 1: **ToC Figure.** A design strategy for reconfigurable metasurfaces exhibiting spatiotemporally programmable textural morphing under simple control is proposed. Viscoelastic shells that can temporarily stay concave before recovering the initial convex state without external loads are chosen as unit cells. Integrating such shells with broadly tuned recovery time by geometry and material viscoelasticity, we create metasurfaces exhibiting spatiotemporal evolution of patterns and friction.

1. Introduction

A lot of living creatures can dynamically adapt their skin textures for locomotion, signaling, and camouflage. For instance, snakes can actively tilt the ventral scales on their skin to prevent sliding when they climb across a complex terrain (Marvi et al., 2016). As the masters of camouflage, cephalopods are capable of adaptively altering the morphology of skin papillae against the ever-changing background when they move on the seabed (Hanlon, 2007; Allen et al., 2014). These examples have inspired numerous artificial materials and devices with tunable surface textures for a wide range of applications in aerospace (Dayyani et al., 2015; Da Ronch et al., 2017), human computer interaction (Rossignac et al., 2003; Stanley et al., 2016; Hu et al., 2018), and soft robotics (Pikul et al., 2017; Rafsanjani et al., 2018; Lamuta et al., 2019; Wang et al., 2019; Fei et al., 2021; Liu et al., 2021a; Alapan et al., 2020). The actuation for textural morphing relies on either mechanical loads (Dayyani et al., 2015; Da Ronch et al., 2017; Rossignac et al., 2003; Stanley et al., 2016; Hu et al., 2018; Pikul et al., 2017; Rafsanjani et al., 2018; Zhang et al., 2015; Dias et al., 2017; Celli et al., 2018; Park et al., 2019; Siéfert et al., 2019) or embedded stimuli-responsive materials (Fei et al., 2021; Liu et al., 2021a; Alapan et al., 2020; Guseinov et al., 2020; Nojoomi et al., 2018; Boley et al., 2019; Bauhofer et al., 2017; Hajiesmaili and Clarke, 2019; Chen et al., 2018; Liu et al., 2017b; Mao et al., 2015).

Unlike the dynamic textural morphing in nature, most synthetic materials transform into only one targeted surface texture in response to a stimulus. Achieving temporally evolving textures, however, is challenging because it is essential to program the surface in both space and time. A straightforward approach for spatiotemporally programmable textural morphing is utilizing mechatronic systems comprising power supplies, multiple motors or pumps, and electronic control devices (Stanley et al., 2016; Pikul et al., 2017; Fei et al., 2021; Liu et al., 2021a), but these electric and electronic components make the whole system complicated, and thus less robust. An alternative approach is spatially patterning active materials with different temporal responses to defined stimuli (Liu et al., 2021a; Guseinov et al., 2020; Chen et al., 2018; Mao et al., 2015; Liu et al., 2017b). However, the temporal texture evolution is unchangeable once the materials have been made. The design of spatiotemporally programmable textural morphing that can be easily operated and reconfigured on demand is still in its infancy.

Here, we develop a spatiotemporally programmable and reconfigurable metasurface that can achieve time-

dependent textural morphing under simple control. The design of this metasurface requires unit cells with widely tunable temporal responses under a defined stimulus. These unit cells can be assembled into a metasurface with a desired spatiotemporal response. The created metasurface can be easily reconfigured into a new one with different spatiotemporal responses by disassembling and reorganizing the unit cells. One example of such unit cells that we adopt here is a viscoelastic shell which can have convex and concave states (**Figure 1b**), analogous to the extended and retracted states of the papillae on cephalopods’ skin (Figure 1a). The shell can buckle into the concave state when subjected to a pressure load, and recovers the convex state after a certain amount of time when the load is removed (Liu et al., 2021b; Brinkmeyer et al., 2012; Gomez et al., 2019; Urbach and Efrati, 2020). The recovery time can be widely tuned by the geometry and viscoelasticity of the shell (Brinkmeyer et al., 2012). As a result, a metasurface comprising the shell units with different recovery time can exhibit pre-programmed temporal texture evolution, which can be easily reconfigured by rearranging the shell units (Figure 1c-d). The proposed metasurfaces are used to display temporal evolution of patterns, such as digit numbers and emoji, and programmed spatiotemporal friction control.

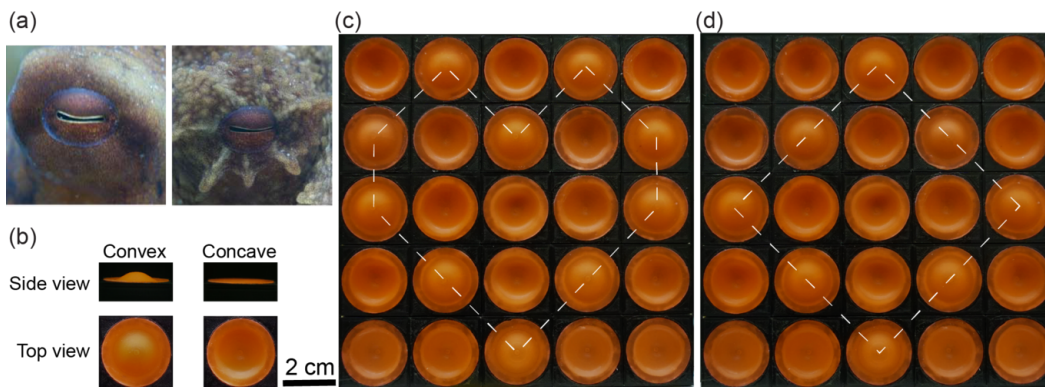


Figure 2: **Figure 1.** Spatiotemporally programmable metasurfaces inspired by the skin papillae in cephalopods. (a) Cephalopods can alter their appearance for camouflage by changing the morphology of their skin papillae. Reproduced with permission. (Allen et al., 2014) Copyright 2013, Wiley Periodicals, Inc. (b) As the unit cell of the metasurfaces, a viscoelastic shell can have two states: convex and concave, analogous to the extended and retracted states of the papillae of cephalopods. The convex shell can be pneumatically actuated to the concave state, and recover the initial convex state after a certain amount of time when the load is removed. (c-d) By arranging the shells of different recovery time, metasurfaces can be formed to exhibit pre-programmed spatiotemporal textural morphing. The metasurfaces can be easily disassembled and rearranged to new ones with different spatiotemporal responses. A “heart” texture shown in (c) can be reconfigured into a “tilted square” texture in (d) by simply reorganizing the shell units.

2. Results and Discussion

2.1 Design of viscoelastic shells with tunable recovery time

Consider viscoelastic shells of revolution with the following profile of the internal surfaces (**Figure 2a**)

$$h(r) = (H - d) \left[1 - 10 \left(\frac{r}{R} \right)^3 + 15 \left(\frac{r}{R} \right)^4 - 6 \left(\frac{r}{R} \right)^5 \right],$$

where H is the height, d is the thickness, and R is the radius of the shell. Such geometry ensures $\frac{dh}{dr} = 0$

and $\frac{d^2h}{dr^2} = 0$ at both the center ($r = 0$) and the edge ($r = R$) of the shell to facilitate the implementation of the boundary conditions in both simulations and experiments. Subjected to clamped boundary conditions and a pressure load Δp , the shell can buckle into a concave shape (dashed lines), yielding a displacement w at its center.

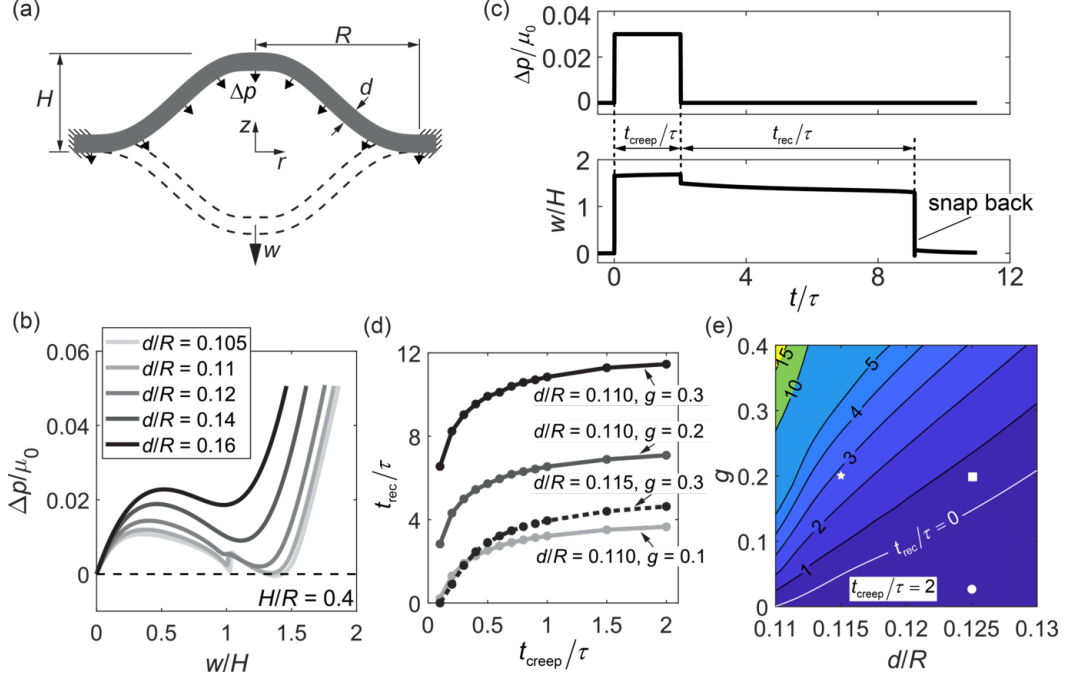


Figure 3: Figure 2. Numerical study of viscoelastic shells with tunable recovery time. (a) Geometry of the shells. The shell is defined by its thickness d , radius R , and height H . The shell can buckle into a concave shape (dashed lines) under a pressure load Δp , yielding a displacement w at its center. (b) The normalized pressure-displacement relations for the shells with $H/R = 0.4$ and different d/R ranging from 0.105 to 0.16 under instantaneous loading. The curves intersecting $\Delta p/\mu = 0$ (dashed line) correspond to bistable shells. (c) Applied pressure-time relation and the corresponding evolution of the displacement over time for the shell with $d/R = 0.11$, $H/R = 0.4$, and $g = 0.2$. The time period when a constant pressure is held is defined as the creeping time t_{creep} , while the time period when the shell stays concave after the pressure is removed is defined as recovery time t_{rec} , which are both normalized by the relaxation time constant of the viscoelastic material τ . (d) The effect of t_{creep}/τ , d/R , and dimensionless relaxation modulus g on t_{rec}/τ . (e) Contour of t_{rec}/τ with respect to g and d/R when $t_{creep}/\tau = 2$. The area underneath the white line corresponds to zero recovery time. The circular, square and pentagram white markers represent the predictions for the viscoelastic shells with zero, intermediate, and long recovery time in the experiments, respectively.

We first conducted finite element analyses (FEA) to study the viscoelastic responses of such shells upon pressure loads using the commercial package Abaqus/Standard (Method). The instantaneous constitutive behavior of the shells is modeled as an incompressible neo-Hookean material with the instantaneous shear modulus μ_0 (Supplementary Text 1). The relaxation of the shear modulus over time t , is described by the Prony series,

$$\mu(t) = \mu_0 \left[1 - \sum_{i=1}^n g_i (1 - e^{-t/\tau_i}) \right],$$

where n is the number of the series terms, μ_0 is the dimensionless relaxation modulus, and τ_i is the relaxation time constant. Only the first term of the Prony series is considered in the FEA with the relaxation parameter and relaxation time constant τ .

We first investigate the instantaneous responses the shells. The normalized pressure $\Delta p/\mu_0$ increases, decreases, and increases again with the normalized displacement w/H for the shells with $H/R = 0.4$ and different d/R ranging from 0.105 to 0.16 (Figure 2b). We find that the $\Delta p/\mu_0 - w/H$ curves for thick shells with $d/R > 0.11$ stay above the horizontal line of zero pressure, indicating that these shells are monostable. As d/R decreases below 0.11 ($d/R = 0.105$), the $\Delta p/\mu_0 - w/H$ curves intersect with the horizontal line of zero pressure, indicating that the shells are bistable. The monostable shells can instantaneously recover from their concave shapes once the pressure load is removed, whereas the bistable shells can stay concave without a pressure load.

Monostable viscoelastic shells are capable of temporarily staying concave for a certain amount of time before recovering to their convex state, even though the pressure load is removed. This phenomenon is called pseudo-bistability (Liu et al., 2021b; Brinkmeyer et al., 2012; Gomez et al., 2019; Urbach and Efrati, 2020), and will be utilized to build metasurfaces with programmable spatiotemporal textural morphing. To quantify the phenomenon in FEA, we instantaneously imposed a pressure load $\Delta p/\mu_0 = 0.03$ on a viscoelastic shell with $H/R = 0.4$, $d/R = 0.11$, and $\nu = 0.2$, and released the pressure after holding it for 2τ (Figure 2c). The corresponding displacement w -time t relation was computed. As a result, the shell immediately snaps into a concave shape once the pressure is applied, and creeps with a small displacement increase $w/H = 0.0326$ for $t_{\text{creep}} = 2\tau$ during the loading. As the pressure is removed, the shell temporarily stays concave for $t_{\text{rec}}/\tau = 7.1$ with w/H slightly decreasing prior to snapping back to the convex state (Figure 2c).

Next, we investigate the effect of loading history, geometry and viscoelasticity on the recovery time t_{rec}/τ . As a result, for the shell with $H/R = 0.4$ subjected to a step pressure load $\Delta p/\mu_0 = 0.03$, t_{rec}/τ increases with t_{creep}/τ , and saturates when $t_{\text{creep}}/\tau = 2$ for a range of d/R and ν (Figure 2d). For a given t_{creep}/τ , a larger ν leads to a longer t_{rec}/τ . We also find that t_{rec}/τ is considerably reduced when the shell becomes thicker (Figure 2d). These trends can be seen more clearly in the contour plot of t_{rec}/τ with respect to d/R and ν when $t_{\text{creep}}/\tau = 2$ (Figure 2e); t_{rec}/τ increases as ν increases or d/R decreases. The growth rate of t_{rec}/τ with respect to ν is dramatically increased as d/R approaches 0.11, which is the boundary demarcating the monostable and bistable shells. The shells corresponding to the region underneath the white line in this contour have a zero recovery time, indicating that they snap back immediately once the pressure load is removed. We note that $\Delta p/\mu_0$ can increase t_{rec}/τ , but this increase is negligible compared to the effects of t_{creep}/τ , and d/R (Figure S2).

2.2 Experimental characterization of viscoelastic shells

Having identified how the recovery time is tuned by the loading history, geometry and viscoelasticity, we now fabricate viscoelastic shells with different recovery time. We selected two materials that have similar moduli but very different viscoelastic properties: silicone rubber (Dragon SkinTM 30, D30) and urethane rubber (VytaFlexTM 20, V20). We conducted stress relaxation tests for these two rubbers and fitted the two-term Prony series to the data, the results of which are given in **Table 1** (Method and Supplementary Text 1). We find that the silicone rubber D30 is highly hyperelastic whereas the urethane rubber V20 is highly viscoelastic, since their moduli decay by 5.08% and 36.71%, respectively, as time approaches infinity.

The two terms in the Prony series for both materials have quite different time constants. Since the creeping time we apply in the experiments is comparable to τ_1 , the pseudo-bistable behavior of the shells is also dominated by the relaxation over a time scale comparable to τ_1 . Therefore, in the following we only consider the first term in the Prony series.

	μ_0 (kPa)	g_1	τ_1 (s)	g_2	τ_2 (s)
Dragon Skin TM 30 (D30)	281	0.03	3.39	0.03	93.8
VytaFlex TM 20 (V20)	172	0.2	4.42	0.16	100.13

Table 1: **Table 1.** Viscoelastic properties of the silicone and urethane rubbers obtained by stress relaxation tests.

We prepared the following four types of viscoelastic shells: bistable shells and the shells with zero, medium, and long recovery time. All the shells have the same radius $R = 10$ mm and height $H = 4$ mm. The thicknesses and materials for the shells of these four types are summarized in **Table 2**. The predicted recovery time for the shells with zero, medium and long recovery time by FEA is marked by a circle, square and pentagram in Figure 2e, respectively. Each shell was fabricated by molding, and was bonded onto a hollow substrate made of polylactic acid (PLA), forming a shell unit, as shown in **Figure 3a**. To diminish the influence of geometric imperfections on the pseudo-bistability (Liu et al., 2021b), the molds for the shells were 3D printed with high resolution (0.06 mm), and a step structure was used to ensure the concentricity between the shell and the substrate (Method, Figure S3-S5). Arrange the shell units in a grid pattern to form a metasurface, for example a 4-by-3 grid (Figure 3b and Figure S6a), where each row corresponds to one type of viscoelastic shells. The shell units are interconnected via tubing so that the pressure loads exerted on them are always the same (Figure S6b). To avoid the disturbance of one shell’s snap motion to other shells’ recovery, the volume of the chamber in the hollow substrate is selected to be more than 20 times of the volume change when one shell snaps from the concave state to the convex state (Method).

Type	d/R	materials
Bistable shells	0.11	Dragon Skin TM 30 (D30)
Shells with $t_{rec} = 0$	0.13	Dragon Skin TM 30 (D30)
Shells with a medium t_{rec}	0.13	VytaFlex TM 20 (V20)
Shells with a long t_{rec}	0.12	VytaFlex TM 20 (V20)

Table 2: **Table 2.** Four types of viscoelastic shells

We build a pneumatic actuation system to extract, hold and release air (Figure 3c). This system contains three vacuum pumps connected in parallel, two 3-way solenoid valves, and a pressure sensor (Method and Figure S7). All the shell units are connected to this system in a way that the tubing lengths from all the shell units to the pumps are equal (Figure S6b). Initially, the two solenoid valves are deactivated, and the pump can rapidly extract air from all the shell units, yielding a pressure load. Once the pressure reaches a targeted value, valve 2 is activated so that the pressure can be held. After a certain amount of creeping time t_{creep} , valve 1 is activated to release the pressure. We connected the metasurface in Figure 3b to this pneumatic actuation system, and prescribed a 7 kPa pressure load ($\Delta p/\mu_0 = 0.0249$ for D30, $\Delta p/\mu_0 = 0.0407$ for V20) for $t_{creep} = 10$ s. Figure 3d shows the evolution of the measured pressure over time. Due to slight leakage, the pressure during the holding process decays from 8.59 kPa to 5.52 kPa ($\Delta p/\mu_0$ reduces from 0.0306 to 0.0196 for D30, from 0.0499 to 0.0321 for V20), yielding an average pressure around 7 kPa. Despite the time-varying pressure, the recovery time t_{rec} of each shell unit can still be well-controlled, since t_{rec} is not sensitive to the applied pressure (Figure S2).

Next, we experimentally characterize the recovery time t_{rec} of the viscoelastic shells. In each measurement, we fixed the average pressure load to be around 7 kPa during the holding process while changed the creeping

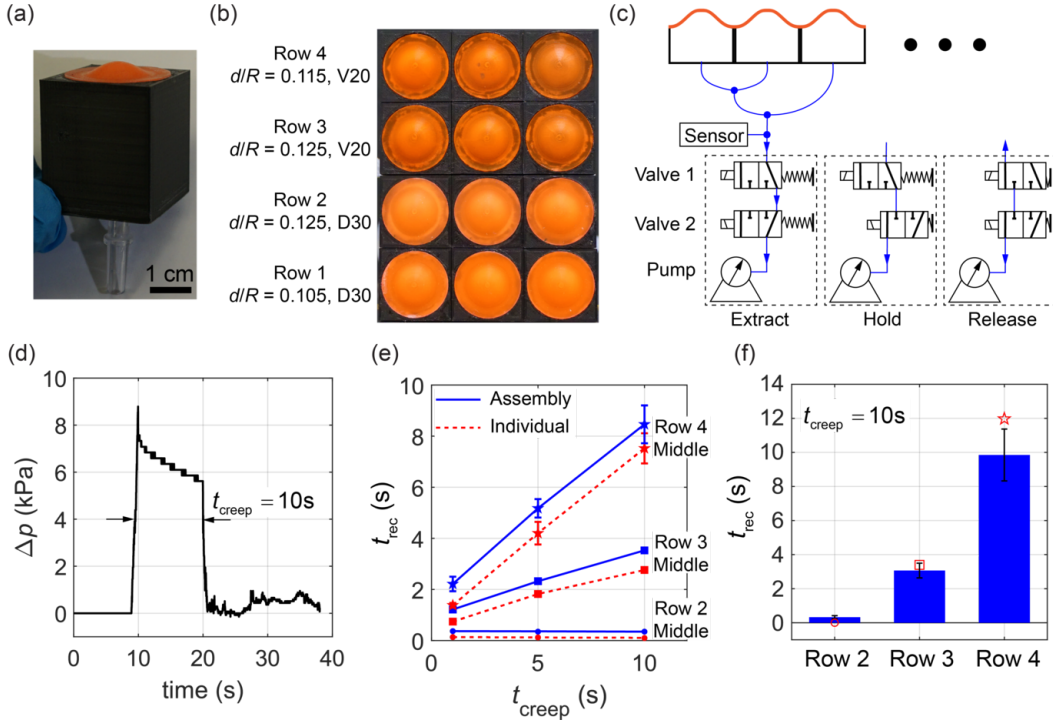


Figure 4: **Figure 3.** Experimental characterization of viscoelastic shells. (a) Snapshot of a shell unit comprising a viscoelastic shell bonded to a hollow substrate made of PLA. (b) A metasurface with 12 shell elements arranged in 4 rows and 3 columns; each row corresponds to one type of shells with different geometry or materials from those in other rows. The shells in row 1 and 2 are made of Dragon SkinTM 30 (D30), and the shells in row 3 and 4 are made of VytaFlexTM 20 (V20). The shells in row 1 are bistable. The shells in row 2, 3, and 4 have zero, medium, and long recovery time, respectively. (c) Schematic of the pneumatic actuation system for extracting, holding and releasing air, where the blue lines represent air flow. (d) Evolution of the measured pressure over time when the metasurface in (b) is actuated by the pneumatic actuation system in (c). (e) The dependence of the recovery time t_{rec} on the creeping time t_{creep} . The blue solid lines represent the results of a shell when it is actuated within the metasurface in (b), whereas the red dashed lines represent the results when the same shell is actuated individually. (f) Histogram of the average t_{snap} in each row of the metasurface when $t_{\text{creep}} = 10$ s. The red hollow markers represent the numerical predictions obtained from Figure 2f. The error bars indicate the standard deviations of the measurements.

time t_{creep} , and determined the t_{rec} using a camera (Method). We first individually actuated the middle shells in row 2-4 of the metasurface in Figure 3b, and measured the average of t_{rec} in five trials for $t_{\text{creep}} = 1$ s, 5 s, 10 s (red dashed lines in Figure 3e). We find that the middle shells in row 2, 3, and 4 have almost zero, medium, and long t_{rec} , respectively, which agrees with the predictions from FEA (Figure 3f). t_{rec} for the middle shell in row 2 keeps nearly zero despite the increase in t_{creep} , whereas t_{rec} for the middle shells in row 3 and 4 increase with an increasing t_{creep} . To check whether t_{rec} of a shell is changed when it is connected in an assembly, we actuated the metasurface shown in Figure 3b, and measured t_{rec} of the middle shells for different t_{creep} (blue solid lines in Figure 3e). We find that the $t_{\text{rec}}-t_{\text{creep}}$ curves are only slightly shifted up for the shells connected in the metasurface. This is caused by the longer time it takes the air to flow into the metasurface than that in a single shell unit after the pressure is released, given that the metasurface has a chamber volume 12 times larger than a shell unit. Figure 3f summarizes the average t_{rec} for row 2, 3, and 4 when the metasurface is actuated for $t_{\text{creep}} = 10$ s (Movies S1), and compares the results with the corresponding numerical predictions. The experimental and FEA results match reasonably

well. From Movie S1, we can clearly see that the shells in row 1 stay concave, whereas the shells in row 2, 3, and 4 snap back sequentially after the pressure is released.

2.3 Metasurfaces exhibiting programmable temporal evolution of patterns

So far, we have identified via simulations and experiments four types of shell units: bistable shells and the shells with zero, medium and long recovery time t_{rec} . Next, we use these shell units as building blocks to create metasurfaces, which can display programmed patterns that evolve over time. To make the shells in the convex and concave states look more different, a piece of black thin paper with a hole is placed on the top of the shells (Figure S5). This cover is so flexible that it does not affect the snap motion of the shell. We first assembled 15 shell units into a 5-by-3 metasurface (**Figure 4a**), in which 2 shell units are bistable, 11 shell units have zero t_{rec} , 1 shell unit has medium t_{rec} , 1 shell unit has long t_{rec} . We instantaneously applied an average pressure around 7 kPa, held this pressure for $t_{\text{creep}} = 10$ s, and quickly released the pressure (similar to Figure 3d). At $t = 0.33$ s after the pressure is released, the shells with a zero t_{rec} snap from the concave state to the convex state, showing a digit number “5”. At $t = 2.57$ s, the shell with a medium t_{rec} recovers, showing a digit number “6”. At $t = 9.33$ s, the shell with a long t_{rec} recovers, showing a digit number “8” (Figure 4a and Movies S2). The metasurface can be easily reconfigured into a 5-by-5 metasurface (Figure 4b), in which 11 shell units are bistable, 9 shell units have zero t_{rec} , 2 shell units have medium t_{rec} , 3 shell units have long t_{rec} . We used the same pressure load to actuate this new metasurface, and observed sequentially a smiley emoji at 0.30 s, a winking emoji at 2.97 s, and an astonished emoji at 11.03 s (Figure 4b and Movies S3).

2.4 Metasurfaces with programmable spatiotemporal friction

Besides displaying temporally programmable patterns, the metasurface can also exhibit spatiotemporal control of friction. When a single shell unit is in contact with a flat rigid plate, the friction at the interface depends on the convexity state of the shell. If the shell is concave, the plate is in contact with the PLA substrate, yielding a low friction. Otherwise, if the shell is convex, the friction is relatively high since the plate is in contact with the rubber (**Figure 5b**). Therefore, a metasurface comprising multiple shell units is capable of spatiotemporally tuning its friction by switching the states of the shell units.

We assembled a 4-by-3 metasurface composed of the four types of shell units. An acrylic board together with a weight (total weight 0.424 kg) was placed on this metasurface, and pulled forward at a constant velocity of 2 mm/s using an Instron testing machine (Model 5944) (Figure 5a, Figure S8). The effective frictional coefficient μ is given by the pulling force F divided by the normal force (4.16 N) exerted on the metasurface. While the board is pulled forward, the metasurface is subjected to a pressure load history in which an average pressure around 7 kPa is applied instantaneously, then held for $t_{\text{creep}} = 10$ s, and released (similar to that in Figure 3d). Accordingly, μ is high before the pressure load is applied when all the shell units are in the convex state. Then μ drops sharply and maintains low for $t_{\text{creep}} = 10$ s, since all the shells become concave due to the pressure load (Figure 5c). Depending on the types of the shell units in the metasurface, μ evolves quite differently over time after the pressure is released. When all the shell units have zero recovery time t_{rec} , they snap immediately after the pressure is released. Correspondingly, μ quickly recovers the value before the pressure load is applied (black line in Figure 5c). When all the shell units are bistable, they stay concave even though the pressure is released. Thus, μ remains low (blue line in Figure 5c). When the metasurface is a mixture of the four types of shell units, where each row corresponds to one type (Figure S8a), μ exhibits a multi-step function of time after the pressure is released (red line in Figure 5c), in which the first, second, and third steps correspond to the recovery of the shell units with zero, medium, and long t_{rec} , respectively. Since the bistable shell units stay concave, the number of shell units in contact with the acrylic board is less than that before the pressure load is applied, and thus μ does not fully recover. We also find that the first step has a larger increase in μ than the other two steps, because the 3 shell units snapping back first bear the whole weight, leading to a larger contact area and thus a higher friction at the interface.

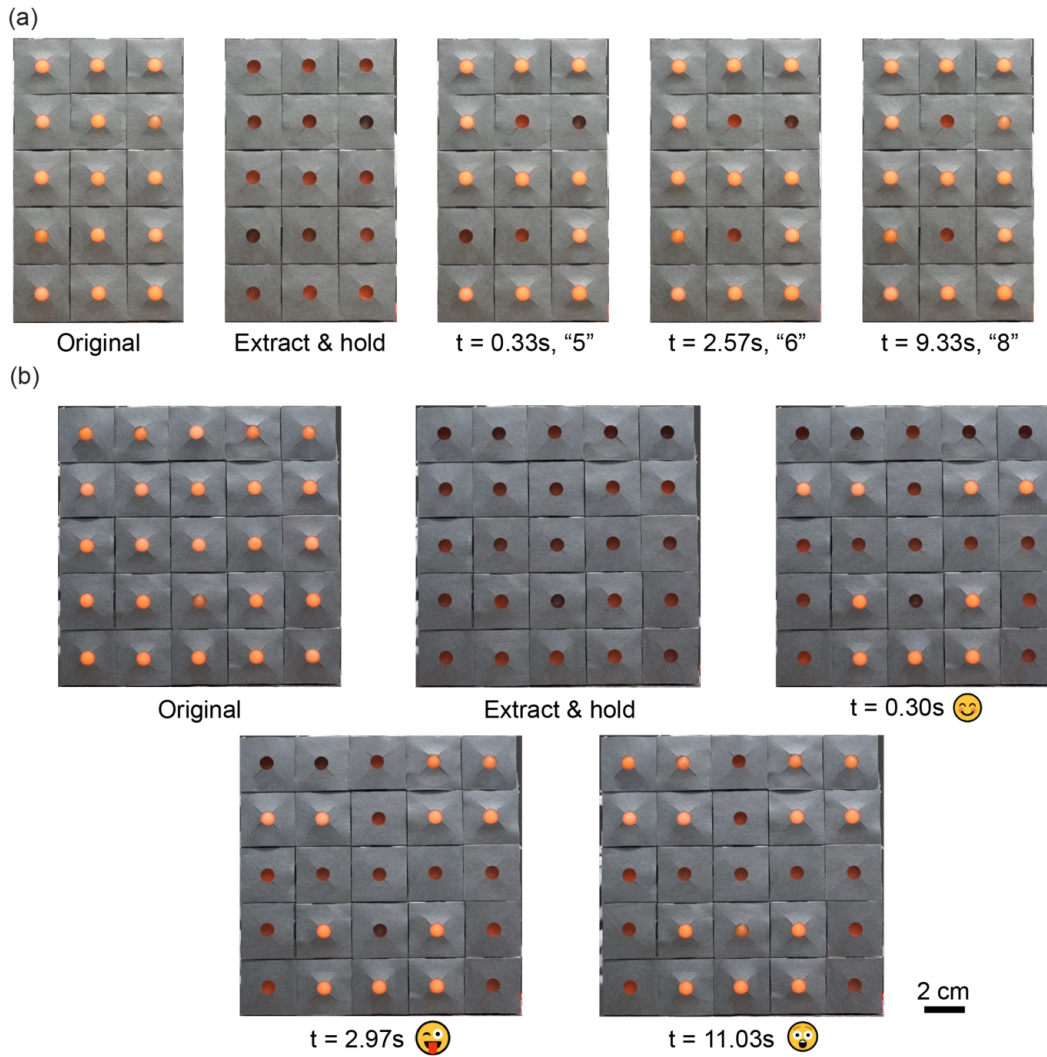


Figure 5: **Figure 4.** Metasurfaces exhibiting temporal evolutions of patterns. (a) The metasurface shows sequentially a digit number "5" at 0.33 s, "6" at 2.57 s, and "8" at 9.33 s. (b) Another metasurface displays different emoji in order of time: a smiley emoji at 0.30 s, a winking emoji at 2.97 s, and an astonished emoji at 11.03 s.

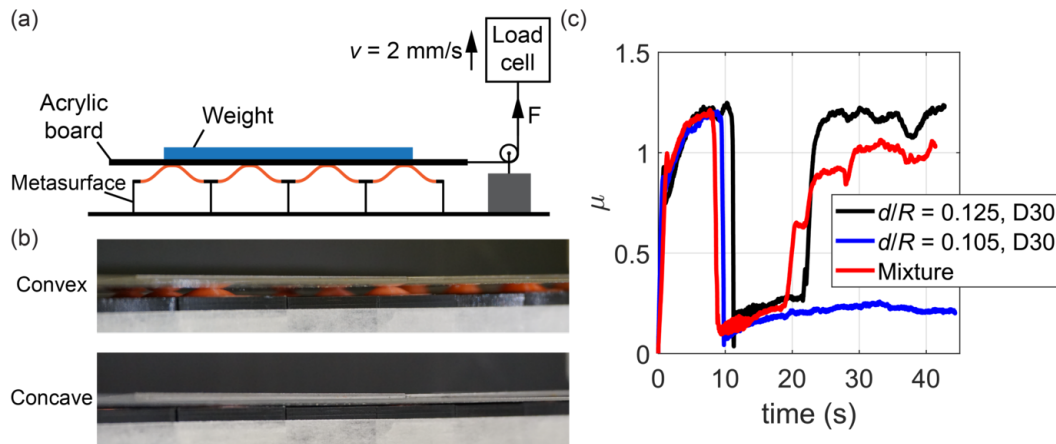


Figure 6: **Figure 5.** Metasurfaces with programmable spatiotemporal friction. (a) Schematic of the experimental setup to measure the effective frictional coefficient between an acrylic board and a metasurface. The acrylic board together with a weight is placed on the metasurface. The load cell pulls the acrylic board at a constant velocity $v = 2 \text{ mm/s}$ and records the resultant pulling force F . (b) When the shells are convex (top), the acrylic board contacts the rubber shells, yielding high friction. When the shells are concave (bottom), the acrylic board contacts the PLA substrate, yielding low friction. When the convexity of the shells spatiotemporally evolves, the frictional property of the metasurface also varies. (c) The effective frictional coefficients μ as functions of time for metasurfaces with 12 shell units arranged in 4 rows and 3 columns. The black and blue solid lines represent the metasurfaces in which all the 12 shell units have zero recovery time, and are bistable, respectively. The red solid line represents the one with a mixture of bistable shells and shells with zero, medium and long recovery time.

3. Conclusion

In summary, we propose a new design strategy for reconfigurable metasurfaces that can exhibit spatiotemporally programmable textural morphing with simple control. The metasurfaces are created by assembling an array of unit cells with tunable temporal responses, and can be reconfigured on demand by disassembling and reorganizing the unit cells. Here we adopt viscoelastic shells as the model unit cells, which can be pneumatically actuated to a concave state, and snap back to the convex state after a certain amount of time when the load is removed. Combining numerical simulations and experiments, we find that the recovery time of those shells can be broadly tuned by the geometry and viscoelastic property of the materials. Using the shell units with different recovery time, we create metasurfaces that can display pre-programmed temporal evolution of patterns, such as digit numbers and emoji. We also demonstrate that the metasurfaces can exhibit spatiotemporal evolution of friction.

The proposed spatiotemporally programmable metasurfaces open the door to a wide range of potential applications. For example, the metasurfaces could be employed as next-generation intelligent reflective roofs (Pisello, 2017). The roof made of the metasurfaces can change its solar reflectance over time by tuning its surface texture such that it reflects less light in the morning and evening, and more at noon. Besides, the metasurfaces could be programmed to have spatiotemporal wetting and adhesion properties (Liu et al., 2017a). The metasurfaces could also be used to achieve spatiotemporally programmable electrical or thermal conductivity at interfaces by manipulating contact.

Experimental Section/Methods

Finite element simulations

To investigate the behaviors of our viscoelastic shells in response to the pressure loads, we performed finite element analysis using the commercial software Abaqus/Standard. We first conducted the simulations for instantaneous loading. The incompressible Neo-hookean material was used to define hyperelastic behavior of the shells. Riks method was implemented to capture the complete equilibrium pressure-displacement responses. We then conducted simulations for time-dependent loading using dynamic implicit method. The single-term Prony series was used to describe the viscous behavior of the shells. Numerical damping with moderate dissipation was applied to reduce the noise to the solution caused by the rapid snap motion. In all the simulations, we constructed axisymmetric shell models and meshed them using hybrid quadratic rectangular elements (Abaqus type CAX8H). We imposed a fixed boundary condition on the edge of the shells.

Stress relaxation tests

Stress relaxation tests were performed to determine the viscoelastic properties of the silicone rubber (Dragon SkinTM30) and urethane rubber (VytaFlexTM 20). A thin film specimen of length 80 mm, width 20 mm, and thickness 2 mm was fabricated by molding for each material, with 1% by weight of IgniteTM orange pigment. An Instron testing machine (Model 5944) equipped with a 50 N loading cells was used for the tests. In the relaxation tests, a 20% tensile strain was applied within 0.5 s and maintained for 300 s. The relations between the resultant forces and time were recorded. A two-term Prony series was fitted to the experimental data using the least-square approach to determine the viscoelastic properties of the materials. We find that the two-term Prony series is sufficient for an accurate fit (the root-mean-square error is less than 0.6%). More details on curve fitting are provided in Supplementary Text 1.

Fabrication of viscoelastic shell units

The shells are made of silicone rubber (Dragon SkinTM30) and urethane rubber (VytaFlexTM 20), with 1% by weight IgniteTM orange pigment. We casted the materials into PLA two-part molds, which were printed by a Ultimaker S5 printer with resolution (layer height) 0.06 mm. The inner surfaces of the molds

for urethane shells were coated with Universal™ Mold Release to facilitate demolding. All the shells have a radius $R = 10$ mm and height $H = 4$ mm. Their thickness d is varied from 1.05 mm to 1.25 mm. The shells at their edges have a flange of width 3 mm. The change in volume of a shell from its concave state to convex state is 528.66 mm^3 when $d = 1.05$ mm and 492.82 mm^3 when $d = 1.25$ mm. After the shells are made, they were glued onto a hollow substrate by applying super glues onto the flanges of the shells. The substrate was made of PLA and 3d-printed in the same way as the molds. The chamber in the substrate is a cylindrical void of radius 10 mm and height 34 mm, yielding a volume 10681 mm^3 . The change in volume caused by the snap motion is less than 5% of the volume of the chamber, and thus, the snapping of one shell does not influence the recovery of others. More details on the fabrication of the shell units are provided in Supporting Information.

Pneumatic actuation system

A pneumatic actuation system was built for extracting air from the shell units, and holding and releasing the pressure. This system consists of three vacuum pumps connecting in parallel (2.1 L/min), two 3-way miniature solenoid valves, an Arduino microcontroller, a power supply, and a pressure sensor (Panasonic, ADP5101) (Figure S7). We used a camera (Sony Alpha a6000, 60fps) to record the snap motion of the shells. When the pressure is released, a 5 mm LED red lamp is turned on to start timing.

Acknowledgements

This work is supported by the startup fund from Henry Samueli School of Engineering and Applied Science at the University of California, Los Angeles (UCLA), and National Science Foundation through a CAREER Award No. CMMI-2048219. This work used computational and storage services associated with the Hoffman2 Shared Cluster provided by UCLA Institute for Digital Research and Education's Research Technology Group.

Conflict of interest

The authors declare no conflict of interest.

Supporting Information

Supporting Information is available in this DOI: [10.22541/au.164019294.41775557/v1](https://doi.org/10.22541/au.164019294.41775557/v1).

References

- Yunus Alapan, Alp C Karacakol, Seyda N Guzelhan, Irem Isik, and Metin Sitti. Reprogrammable shape morphing of magnetic soft machines. *Science advances*, 6(38):eabc6414, 2020.
- Justine J Allen, George RR Bell, Alan M Kuzirian, Sachin S Velankar, and Roger T Hanlon. Comparative morphology of changeable skin papillae in octopus and cuttlefish. *Journal of morphology*, 275(4):371–390, 2014.
- Anton A Bauhofer, Sebastian Krödel, Jan Rys, Osama R Bilal, Andrei Constantinescu, and Chiara Daraio. Harnessing photochemical shrinkage in direct laser writing for shape morphing of polymer sheets. *Advanced Materials*, 29(42):1703024, 2017.

- J William Boley, Wim M van Rees, Charles Lissandrello, Mark N Horenstein, Ryan L Truby, Arda Kotikian, Jennifer A Lewis, and L Mahadevan. Shape-shifting structured lattices via multimaterial 4D printing. *Proceedings of the National Academy of Sciences*, 116(42):20856–20862, 2019.
- A Brinkmeyer, M Santer, A Pirrera, and PM Weaver. Pseudo-bistable self-actuated domes for morphing applications. *International Journal of Solids and Structures*, 49(9):1077–1087, 2012.
- Paolo Celli, Connor McMahan, Brian Ramirez, Anton Bauhofer, Christina Naify, Douglas Hofmann, Basile Audoly, and Chiara Daraio. Shape-morphing architected sheets with non-periodic cut patterns. *Soft matter*, 14(48):9744–9749, 2018.
- Tian Chen, Osama R Bilal, Kristina Shea, and Chiara Daraio. Harnessing bistability for directional propulsion of soft, untethered robots. *Proceedings of the National Academy of Sciences*, 115(22):5698–5702, 2018.
- Andrea Da Ronch, Li Yongchao, Lu Zhang, Roeland De Breuker, Johannes Kirn, Stefan Storm, Li Daochun, Hans Peter Monner, and Markus Kintscher. A Review of Modelling and Analysis of Morphing Wings. *Progress in Aerospace Sciences*, 2017.
- I Dayyani, AD Shaw, EI Saavedra Flores, and MI Friswell. The mechanics of composite corrugated structures: A review with applications in morphing aircraft. *Composite Structures*, 133:358–380, 2015.
- Marcelo A Dias, Michael P McCarron, Daniel Rayneau-Kirkhope, Paul Z Hanakata, David K Campbell, Harold S Park, and Douglas P Holmes. Kirigami actuators. *Soft matter*, 13(48):9087–9092, 2017.
- Fan Fei, Parth Kotak, Li He, Xiaofeng Li, Cyan Vanderhoef, Caterina Lamuta, and Xuan Song. Cephalopod-Inspired Stretchable Self-Morphing Skin Via Embedded Printing and Twisted Spiral Artificial Muscles. *Advanced Functional Materials*, 31(46):2105528, 2021.
- Michael Gomez, Derek E Moulton, and Dominic Vella. Dynamics of viscoelastic snap-through. *Journal of the Mechanics and Physics of Solids*, 124:781–813, 2019.
- Ruslan Guseinov, Connor McMahan, Jesús Pérez, Chiara Daraio, and Bernd Bickel. Programming temporal morphing of self-actuated shells. *Nature communications*, 11(1):1–7, 2020.
- Ehsan Hajiesmaili and David R Clarke. Reconfigurable shape-morphing dielectric elastomers using spatially varying electric fields. *Nature communications*, 10(1):1–7, 2019.
- Roger Hanlon. Cephalopod dynamic camouflage. *Current biology*, 17(11):R400–R404, 2007.
- Yuhan Hu, Zhengnan Zhao, Abheek Vimal, and Guy Hoffman. Soft skin texture modulation for social robotics. In *2018 IEEE International Conference on Soft Robotics (RoboSoft)*, pages 182–187. IEEE, 2018.
- Caterina Lamuta, Honglu He, Kaihao Zhang, Michael Rogalski, Nancy Sottos, and Sameh Tawfick. Digital texture voxels for stretchable morphing skin applications. *Advanced Materials Technologies*, 4(8):1900260, 2019.
- Ke Liu, Felix Hacker, and Chiara Daraio. Robotic surfaces with reversible, spatiotemporal control for shape morphing and object manipulation. *Science Robotics*, 6(53):Art–No, 2021a.
- Mingjie Liu, Shutao Wang, and Lei Jiang. Nature-inspired superwettability systems. *Nature Reviews Materials*, 2(7):1–17, 2017a.
- Tianzhen Liu, Yuzhen Chen, Liwu Liu, Yanju Liu, Jinsong Leng, and Lihua Jin. Effect of imperfections on pseudo-bistability of viscoelastic domes. *Extreme Mechanics Letters*, 49:101477, 2021b.
- Ying Liu, Brandi Shaw, Michael D Dickey, and Jan Genzer. Sequential self-folding of polymer sheets. *Science Advances*, 3(3):e1602417, 2017b.

- Yiqi Mao, Kai Yu, Michael S Isakov, Jiangtao Wu, Martin L Dunn, and H Jerry Qi. Sequential self-folding structures by 3D printed digital shape memory polymers. *Scientific reports*, 5(1):1–12, 2015.
- Hamidreza Marvi, James P Cook, Jeffrey L Streater, and David L Hu. Snakes move their scales to increase friction. *Biotribology*, 5:52–60, 2016.
- Amirali Nojoomi, Hakan Arslan, Kwan Lee, and Kyungsook Yum. Bioinspired 3D structures with programmable morphologies and motions. *Nature communications*, 9(1):1–11, 2018.
- Yujin Park, Gianmarco Vella, and Kenneth J Loh. Bio-inspired active skins for surface morphing. *Scientific reports*, 9(1):1–10, 2019.
- JH Pikul, S Li, H Bai, RT Hanlon, I Cohen, and Robert F Shepherd. Stretchable surfaces with programmable 3D texture morphing for synthetic camouflaging skins. *Science*, 358(6360):210–214, 2017.
- Anna Laura Pisello. State of the art on the development of cool coatings for buildings and cities. *Solar Energy*, 144:660–680, 2017.
- Ahmad Rafsanjani, Yuerou Zhang, Bangyuan Liu, Shmuel M Rubinstein, and Katia Bertoldi. Kirigami skins make a simple soft actuator crawl. *Science Robotics*, 3(15), 2018.
- Jarek Rossignac, Mark Allen, Wayne J Book, Ari Glezer, Imme Ebert-Uphoff, Chris Shaw, David Rosen, Stephen Askins, Jing Bai, Paul Bosscher, et al. Finger sculpting with digital clay: 3d shape input and output through a computer-controlled real surface. In *2003 Shape Modeling International.*, pages 229–231. IEEE, 2003.
- Emmanuel Siéfert, Etienne Reyssat, José Bico, and Benoît Roman. Bio-inspired pneumatic shape-morphing elastomers. *Nature materials*, 18(1):24–28, 2019.
- Andrew A Stanley, Kenji Hata, and Allison M Okamura. Closed-loop shape control of a haptic jamming deformable surface. In *2016 IEEE International Conference on Robotics and Automation (ICRA)*, pages 2718–2724. IEEE, 2016.
- Erez Y Urbach and Efi Efrati. Predicting delayed instabilities in viscoelastic solids. *Science advances*, 6(36): eabb2948, 2020.
- Yunlong Wang, Huanqing Cui, Qilong Zhao, and Xuemin Du. Chameleon-inspired structural-color actuators. *Matter*, 1(3):626–638, 2019.
- Yihui Zhang, Zheng Yan, Kewang Nan, Dongqing Xiao, Yuhao Liu, Haiwen Luan, Haoran Fu, Xizhu Wang, Qinglin Yang, Jiechen Wang, et al. A mechanically driven form of Kirigami as a route to 3D mesostructures in micro/nanomembranes. *Proceedings of the National Academy of Sciences*, 112(38):11757–11764, 2015.